

Showcasing interdisciplinary research from Professor Levin's laboratory, Electrochemistry Department, St. Petersburg State University, Russian Federation as well as Professor Behrends' laboratory, Berlin Joint EPR Lab, Fachbereich Physik, Freie Universität Berlin, Germany.

Spins at work: probing charging and discharging of organic radical batteries by electron paramagnetic resonance spectroscopy

This article reports on the development of a versatile on-substrate electrode setup for spectroelectrochemical Electron Paramagnetic Resonance (EPR) measurements on redox conductive polymers for organic radical batteries. The setup is used to perform quantitative in-operando EPR as well as low-temperature pulse EPR experiments on electrochemical cells with a novel di-TEMPO Ni-Salen polymer as a particularly promising energy-storage material.

### As featured in:



See Jan Behrends *et al.*,  
*Energy Environ. Sci.*, 2022, **15**, 3275.

## PAPER

View Article Online  
View Journal | View IssueCite this: *Energy Environ. Sci.*, 2022, 15, 3275

## Spins at work: probing charging and discharging of organic radical batteries by electron paramagnetic resonance spectroscopy†

Iliia Kulikov,<sup>‡a</sup> Naitik A. Panjwani,<sup>‡a</sup> Anatoliy A. Vereshchagin,<sup>‡b</sup> Domenik Spallek,<sup>a</sup> Daniil A. Lukianov,<sup>b</sup> Elena V. Alekseeva,<sup>‡ab</sup> Oleg V. Levin<sup>‡b</sup> and Jan Behrends<sup>‡a</sup>

Organic radical batteries (ORBs) are a promising class of electrochemical power sources employing organic radicals as redox-active groups. This article reports on the development of a versatile on-substrate electrode setup for spectroelectrochemical Electron Paramagnetic Resonance (EPR) measurements on redox conductive polymers for ORBs. Quantitative *in operando* EPR experiments performed on electrochemical cells with a di-TEMPO Ni-Salen polymer as active electrode material demonstrate a strong decrease in the number of paramagnetic centers upon oxidizing the film. The distinct EPR signatures of the TEMPO-containing polymer and its fragments in different molecular environments are used to study its degradation upon repeated cycling. A comparison between the number of EPR-active sites and the number of electrochemically active charges, as measured by cyclic voltammetry, provides information on the nature of the degradation process. Low-temperature *ex situ* pulse EPR measurements on the oxidized polymer film reveal the spectrum of dilute nitroxide species, which may be associated with electrochemically inactive islands. These experiments pave the way for advanced EPR techniques for accurately determining distances between adjacent paramagnetic centers and thus for identifying performance-limiting loss mechanisms, which can eventually help develop strategies for making ORBs powerful contenders on the path towards sustainable electrochemical power sources.

Received 7th April 2022,  
Accepted 20th June 2022

DOI: 10.1039/d2ee01149b

rsc.li/ees

## Broader context

Storage of electrical energy is a ubiquitous need in our energy-driven society, and efficient batteries are key elements for the indispensable transformation towards a world driven by renewable power sources. The well-established lithium-ion technology exhibits a number of indisputable drawbacks with regard to flexibility, safety and limited resources. These limitations inherent to today's battery technology are fueling the development of alternative materials and concepts for sustainable future energy-storage devices. Batteries with polymer electrode materials containing stable radicals are particularly promising alternatives to conventional lithium-ion batteries. However, the performance of organic radical batteries (ORBs) substantially lags behind their lithium-containing counterparts. A further improvement of ORB technology requires an in-depth understanding of the charging and discharging processes on the molecular level. This is where magnetic resonance techniques can play a key role, as electron spins are unique local probes for elucidating redox reactions in ORBs. The methodological developments reported in this work open up new avenues for tailor-made spin-sensitive techniques for ORB research. Quantitative *in operando* as well as advanced pulse electron paramagnetic resonance experiments can contribute to an efficient identification of loss mechanisms as well as transport-limiting processes and thus help improving the performance of environmentally-friendly alternatives to lithium-ion batteries.

## 1 Introduction

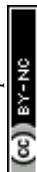
Batteries based on conjugated polymers containing stable radical moieties as high-capacitance groups represent a promising class of future electrochemical power sources.<sup>1–4</sup> They combine the advantages of high-power supercapacitors, namely high discharge rates, and the high energy density of conventional lithium-ion technology. A further beneficial property of

<sup>a</sup> Berlin Joint EPR Lab, Freie Universität Berlin, Fachbereich Physik, Arnimallee 14, D-14195 Berlin, Germany. E-mail: j.behrends@fu-berlin.de

<sup>b</sup> Electrochemistry Department, St. Petersburg State University, 7/9 Universitetskaya nab., St. Petersburg, 199034, Russian Federation

† Electronic supplementary information (ESI) available. See DOI: <https://doi.org/10.1039/d2ee01149b>

‡ These authors contributed equally to this work.





organic materials over traditional inorganic materials is their availability and the low cost of the starting materials for the synthesis of the target polymers in conjunction with good mechanical properties.<sup>5–7</sup>

While active electrode materials with nitroxide radicals as redox-active groups are ideally suited for organic radical batteries (ORBs) that exhibit high power densities, the broad application of most nitroxide-based materials is limited by their moderate electrical properties. A promising route towards overcoming the conductivity problem is the use of polymers that combine radical-containing moieties and a conductive backbone. This strategy was successfully followed in a number of studies focusing on different polymers.<sup>8–13</sup>

Common to all these polymers is the fact that they contain 2,2,6,6-tetramethylpiperidine-1-oxyl (TEMPO) as nitroxide pendant groups. Upon changing the redox state of the TEMPO group, the neutral nitroxide radical (TEMPO<sup>•</sup>) is converted into the hydroxylamine anion (TEMPO<sup>−</sup>) or the oxoammonium cation (TEMPO<sup>+</sup>). Only the neutral radical has an unpaired electron spin ( $S = 1/2$ ) and can thus be detected using Electron Paramagnetic Resonance (EPR) spectroscopy. For this reason EPR is commonly used to detect the presence of radicals in active-electrode materials for ORBs.<sup>1,2,9,12,14,15</sup> The vast majority of EPR studies use continuous wave EPR (cwEPR) measurements merely to confirm the radical nature of the active materials *ex situ*. However, also *in situ* and *in operando* experiments have recently been demonstrated, providing direct access to the change of the redox state upon charging and discharging of ORBs.<sup>16,17</sup> This opens the intriguing perspective of determining yields for charging and discharging processes by means of *in operando* quantitative cwEPR spectroscopy. We note that quantitative cwEPR can accurately assess the absolute number of unpaired electron spins in a given volume with high sensitivity. This has, for instance, been recently used to quantitatively investigate doping of conjugated polymers.<sup>18,19</sup>

Conventional *in operando* cwEPR experiments were previously employed to monitor structural changes at the anode in lithium-ion batteries,<sup>20–23</sup> highlighting the usefulness of *in operando* EPR spectroscopy for battery research in general. The cwEPR spectrum itself contains valuable information on the molecular environment and the local geometry of the spin-bearing groups. For instance, in the case of nitroxide-based materials, the cwEPR spectra of immobilised dilute nitroxides in a solid film, densely packed nitroxides in a thin film, nitroxides in solution and two nitroxides in close vicinity forming a dimer are all well distinguishable.<sup>24,25</sup>

However, *in operando* experiments are by no means restricted to cwEPR measurements. The information content accessible by EPR can substantially be increased further by using modern pulse EPR (pEPR) techniques.<sup>26</sup> Recently, pEPR measurements performed on batteries based on inorganic, lithium-containing electrode materials were reported,<sup>27</sup> clearly showing that pEPR experiments are indeed feasible and can provide insights into the kinetics of processes occurring on the electrodes upon fast charging. The application of pEPR spectroscopy is particularly promising for ORBs with TEMPO-based

active electrode materials, as nitroxide radicals give strong and well-studied EPR signals. In fact, nitroxide radicals are probably the most studied paramagnetic system due to their routine use in EPR-based distance measurements in proteins.<sup>28</sup> Apart from accurately determining distances between neighboring radicals, pEPR techniques can also provide new insights into the wave function localization of paramagnetic states<sup>29</sup> as well as molecular motion of the nitroxide groups.<sup>25,30</sup>

Here we describe the development of an electrochemical cell that allows us to perform *in operando* cwEPR measurements as well as pEPR experiments using conventional EPR resonators. We employ quantitative cwEPR spectroscopy to study charging and discharging processes of a novel, recently synthesized electrode material for ORBs based on a di-TEMPO Ni-Salen polymer (p-DiTS).<sup>31</sup> Our results demonstrate that almost all TEMPO groups can successfully be oxidized and reduced upon changing the potential applied to the cell. The distinct differences between the room-temperature EPR spectra of nitroxide radicals immobilized on the cathode and those dissolved in the electrolyte enable us to explore the influence of various deposition parameters on the stability of the p-DiTS film prepared by electropolymerization. Further, we successfully conduct low-temperature electron spin echo measurements on a fully reduced p-DiTS film. The echo-detected pEPR spectrum exhibits signatures of dilute nitroxide spins, which are possibly associated with electrochemically inactive islands of the film that reduce the cell capacity. Our pEPR results pave the way for systematic potential-dependent electron–electron double resonance (ELDOR) experiments for accurately determining distances between adjacent paramagnetic centers and thus for identifying performance-limiting loss mechanisms.

## 2 Versatile electrode setup for *ex situ* and *in situ* spectroelectrochemical EPR

There is increasing interest in both *ex situ* and *in situ* spectroelectrochemical (SEC) EPR measurements in research fields ranging from biology to materials science, from redox active systems such as proteins<sup>32</sup> and hydrogenase to catalysis,<sup>33–37</sup> redox-flow batteries<sup>38</sup> and of course ORBs.<sup>16,17</sup> One significant drawback with SEC EPR is the fact that microwave resonators suffer from substantial microwave damping as a result of introducing metal electrodes, polar solvents and ionic salts (*i.e.*, the electrolyte) needed for successful electrochemistry.<sup>39</sup> Microwave damping can be significantly reduced by our novel on-substrate electrode design (see Fig. 1(b)) as this limits the amount of metal that is introduced into the resonator, while still allowing us to have electrode surface areas large enough to deposit sufficient material of interest to observe EPR signals.

The on-substrate electrodes are produced as follows. Cleaned quartz substrates are placed inside a holder and covered with shadow masks. The assembly is transferred into a vacuum chamber equipped with a thermal evaporator (MBraun ProVap 5G PVD System). At a pressure of  $7 \times 10^{-7}$  mbar, 10 nm of chromium (Cr) is evaporated as an adhesion layer, followed by



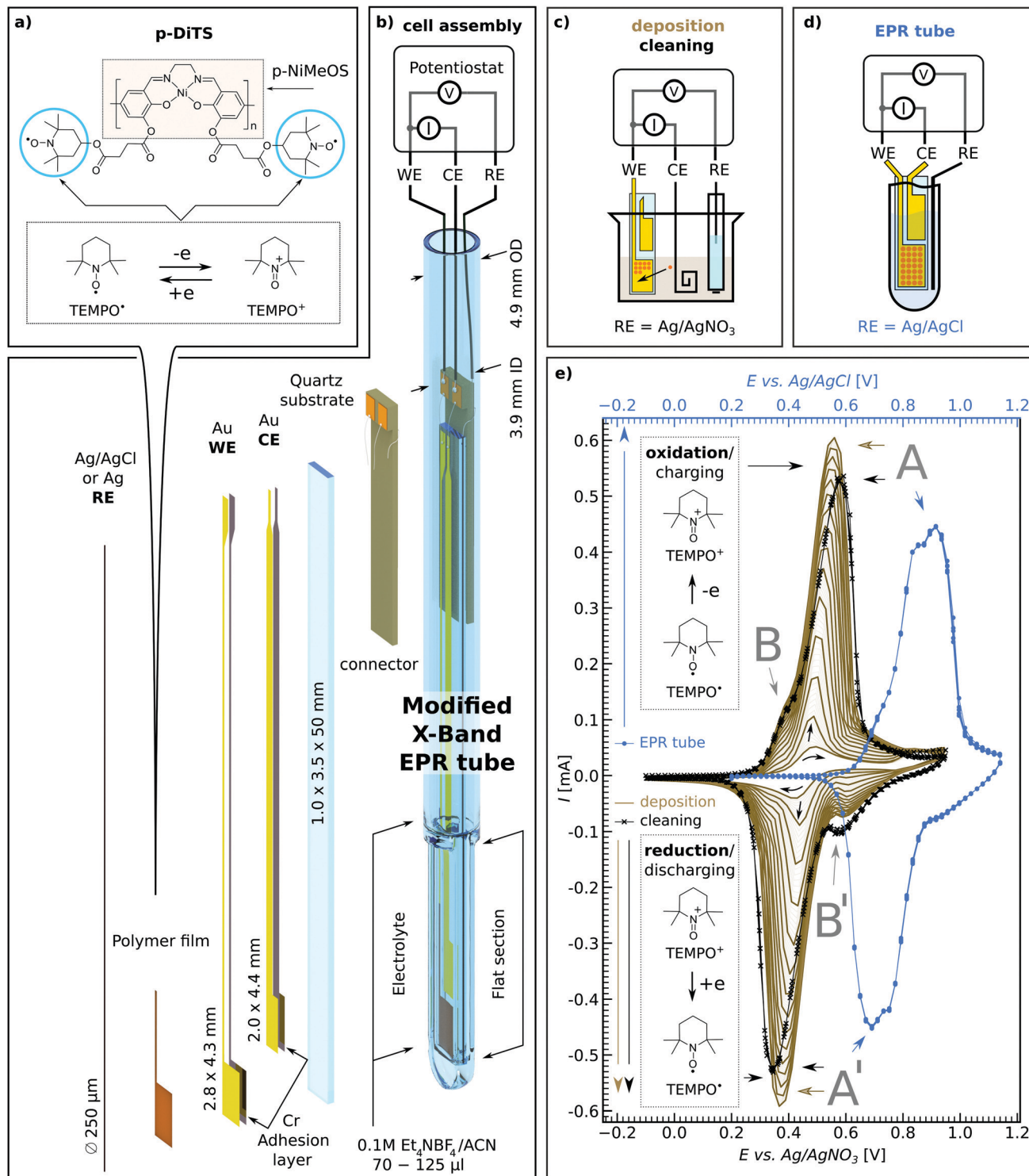


**Fig. 1** Schematic diagram of the electrode design and assembly of the electrochemical cell based on a modified X-band EPR quartz tube. (a) Molecular structure of p-DiTS, with the redox reaction of its charge-bearing TEMPO groups; highlighted is the backbone, p-NiMeOSalen. (b) Assembly of the electrochemical cell in the modified sample tube with a flattened bottom section. (c) Electrochemical setup for deposition and cleaning of polymer films. (d) Tube-based electrochemical setup. (e) Cyclic voltammograms of a growing p-DiTS film during 100 electropolymerization cycles (solid-brown), during the cleaning process (crossed-black) and in the tube-based setup (dotted-blue). Peaks A/A', B/B' correspond to the oxidation and reduction of the TEMPO fragments and of the p-NiSalen backbone, respectively. All CV were recorded at 50  $\text{mV s}^{-1}$ .

180 nm of gold (Au). In this way the on-substrate working and counter electrodes are formed (WE and CE respectively).

The reference electrode (RE) is not evaporated on substrate for electrochemical stability reasons. Instead, a 250  $\mu\text{m}$  Ag wire is



used, either as is or, for additional stability, coated galvanically with a AgCl layer.<sup>40</sup> See Section S1 in the ESI† for details of the sample preparation.

The above procedure provides a WE active area of 12.0 mm<sup>2</sup> which allows one to deposit an electrochemically active film that is large enough to yield a clear EPR signal. The flat electrode design provides the possibility to increase the WE area for samples with particularly small EPR signals while still maintaining certain film thicknesses. This also allows for studying EPR properties as a function of film thickness. In cases where the electrochemical process is thought to deposit material on both the WE and CE, the distance between the on-substrate electrodes can be adjusted such that only one of the electrodes is positioned in the active volume of the microwave resonator, allowing for selective EPR probing of either of the electrodes.

The on-substrate electrodes reduce microwave damping. However, a substantial amount of microwave damping occurs due to the electrolyte, made of polar solvent and ionic salts. Therefore, we further optimize our setup by modifying conventional 5 mm outer diameter (OD) quartz EPR tubes by flattening the bottom 1.3–1.6 cm (*cf.* Fig. 1(b) and Section S1 in the ESI†), thereby reducing the active electrolyte volume needed to submerge both the WE and CE on the substrate as well as the RE wire, from ~120  $\mu$ L to ~60–70  $\mu$ L.

The flattened tube and the thin-film electrode setup have an additional benefit in that the sample is moved away from the maximum of the electric field distribution in the Bruker ER 4122-SHQE resonator (TE<sub>011</sub> mode cavity for cwEPR), thereby further increasing the resonator quality factor (*Q*-factor, given by  $Q = \frac{\nu_{\text{res}}}{\Delta\nu}$ ,  $\nu_{\text{res}}$  = resonance frequency,  $\Delta\nu$  = FWHM of the resonance dip) and hence sensitivity. Further improvements can be made using the flat electrode setup in a TM<sub>110</sub> mode cwEPR cylindrical cavity such as a Bruker ER 4103-TM (developed for studying samples exhibiting high dielectric constants), where the flattened cell can be aligned to further reduce coupling to the microwave electric field. The modified tube is compatible with commercial Bruker ER 4118X-MD5 resonators, most commonly used for advanced pulse EPR measurements at X-band frequencies ( $\nu$  = 9–10 GHz).

## 2.1 Materials

The materials investigated in this study are (1) p-DiTS – a redox-conductive polymer with a NiSalen conductive, conjugated backbone and two charge-bearing redox-active nitroxide radicals (TEMPO) per monomer unit, and (2) polymeric NiMeOSalen (p-NiMeOSalen) which is chemically similar to p-DiTS except for the fact that it does not contain the TEMPO moieties and instead is terminated with a methyl group after the remaining oxygen (see Fig. 1(a) for both molecular structures). The materials were synthesized as previously reported.<sup>31,41,42</sup>

P-DiTS can be anodically electropolymerized from the DiTS monomer dissolved in the electrolyte to form a thin on-electrode film – representing the active cathode material in an ORB. The NiSalen conductive backbone, together with the high concentration

of unpaired electrons (TEMPO radicals), endow p-DiTS films with high specific capacity and fast charge and discharge rates (up to 83 mA h g<sup>−1</sup> at 60C and 31 mA h g<sup>−1</sup> at 3000C, with 66% capacity retention after 2000 charge–discharge cycles).<sup>31</sup> This makes p-DiTS a promising cathode-active charge-storage material capable of high charge–discharge rates.

The TEMPO groups in p-DiTS can undergo a reversible and rapid redox reaction between two stable states,<sup>31</sup> a neutral nitroxide radical (TEMPO•) and an oxoammonium cation (TEMPO<sup>+</sup>), see Fig. 1(a). In the reduced (discharged) state, the TEMPO• moieties of p-DiTS possess unpaired electrons, which makes them paramagnetic and therefore EPR active. In the oxidized (charged) state, the withdrawal of an electron results in a positively charged TEMPO<sup>+</sup>, which is diamagnetic and hence EPR silent. The polymeric NiSalen backbone of p-DiTS (*e.g.*, p-NiMeOSalen) is also known to be redox active and to show potential-dependent EPR signals, which were attributed to the formation of positively charged biphenoxyl radicals by Dmitrieva *et al.*<sup>43</sup> Therefore we study both p-DiTS and p-NiMeOSalen using SEC cwEPR.

## 2.2 Electrochemical polymerization and cyclic voltammetry in a modified EPR tube

The monomeric DiTS is electropolymerized to p-DiTS and simultaneously deposited onto the 12 mm<sup>2</sup> on-substrate Au WE. The setup for deposition is shown in Fig. 1(c). The CE for the deposition is a coiled Pt wire. Both electrodes are submerged in the electrolyte (0.1 M tetraethylammonium tetrafluoroborate (Et<sub>4</sub>NBF<sub>4</sub>) in acetonitrile (ACN)) containing 1 mM monomeric DiTS. The chemically inert RE for the deposition is a Ag wire in a solution of 10 mM AgNO<sub>3</sub> and 0.1 M tetrabutylammonium tetrafluoroborate in ACN, placed inside a glass tube with a porous CoralPor™ tip. A cyclically changing potential between −50 mV and +900 mV is applied between the CE and RE for 8 to 200 deposition cycles, at a rate up to 50 mV s<sup>−1</sup>. The deposition process is monitored by recording a cyclic voltammogram (CV). This results in the deposition of a thin film of p-DiTS on the on-substrate WE. In studies involving NiMeOSalen films, 10 to 20 deposition cycles led to considerably thicker films (~1  $\mu$ m). p-DiTS has lower conductivity than p-NiMeOSalen,<sup>31</sup> therefore the growth of p-DiTS films is hindered after fewer deposition cycles as compared to p-NiMeOSalen. The thicknesses (*t*) of all films used in this study are listed in Section S3 (ESI†). A few representative thicknesses are: for p-DiTS, 8 deposition cycles result in *t* ≈ 40 nm, and 200 deposition cycles result in *t* ≈ 500 nm films; for p-NiMeOSalen, 15 deposition cycles result in *t* ≈ 900 nm.

The most electrochemically stable and pure films came from polymerized systems which were rinsed in ACN followed by propylene carbonate (PC), then rinsing the charged film (900 mV with respect to the Ag/AgNO<sub>3</sub> RE) in a beaker-based cell, and lastly potential-cycling it in the electrolyte. The effects of rinsing and cycling of the polymer films in solvents/electrolyte are described in Section 3.2.1.

There are some differences in the CV recorded in a beaker (setup schematic in Fig. 1(c)) as compared to the CV measured



in the modified tube (setup schematic in Fig. 1(d)). As seen in Fig. 1(e), the CV measured in the modified tube (blue curve) shows slightly shifted and broader oxidation and reduction peaks as compared to the in-beaker measurements (solid-brown and crossed-black curves) for the same p-DiTS film. The shift is mainly due to the use of different reference electrodes, while we attribute the broader peaks to the smaller electrolyte volume used in the modified tube. The electrolyte volume seen by the on-substrate films in the modified tube is significantly smaller than the total electrolyte volume of 60–70  $\mu\text{L}$ , as only 0.35 mm of space remains between the inner width of the flattened modified tube and the substrate. Hence, not more than a 0.2 mm layer of electrolyte is seen by the films. The CV in a modified tube shows less distortions with slower scan rates (*e.g.* 5  $\text{mV s}^{-1}$  used for studies in Section 3.3) and also with higher concentrations of the electrolyte, as the former gives more time for the ion diffusion and the latter improves the ionic conductivity of the electrolyte. While the CV in the modified tube is distorted, the oxidation and reduction peaks remain symmetric, suggesting that the reversibility of the redox process is not hindered.

### 2.3 EPR-active states in p-DiTS-based electrochemical cells

EPR spectra of electrochemical cells with p-DiTS as active-electrode material can exhibit a variety of different signals. Before presenting

and discussing the experimental results, we will provide an overview about the various characteristic cwEPR lineshapes associated with nitroxides in different environments.

Fig. 2(a) shows the spectrum expected for a densely packed p-DiTS film with all nitroxides in the EPR-active reduced state. The broad unstructured line results from the strong dipolar and exchange interaction between both nitroxides of each DiTS monomer as well as between the nitroxides of different monomers. The exchange interaction can lead to either line narrowing or broadening depending on the strength of the interaction,<sup>44</sup> while the dipolar interaction causes broadening. In consequence, the overall cwEPR line width depends on the spin concentration in the film.

Dilute mono-TEMPO fragments dissolved in the electrolyte, each containing only one nitroxide, give rise to a three-line spectrum (*cf.* Fig. 2(b)) which is well known from nitroxide-based spin labels in solution.<sup>45</sup> Tumbling of the molecules in the liquid electrolyte results in an averaging of the anisotropic interaction between the electron spin and the nitrogen nuclear spin ( $I = 1$ ) as well as of the  $g$  anisotropy, leaving only the isotropic part of the hyperfine coupling and the isotropic  $g$ -value.

Dilute DiTS monomers in the electrolyte generally give a spectrum consisting of five narrow lines (*cf.* Fig. 2(c)), if each

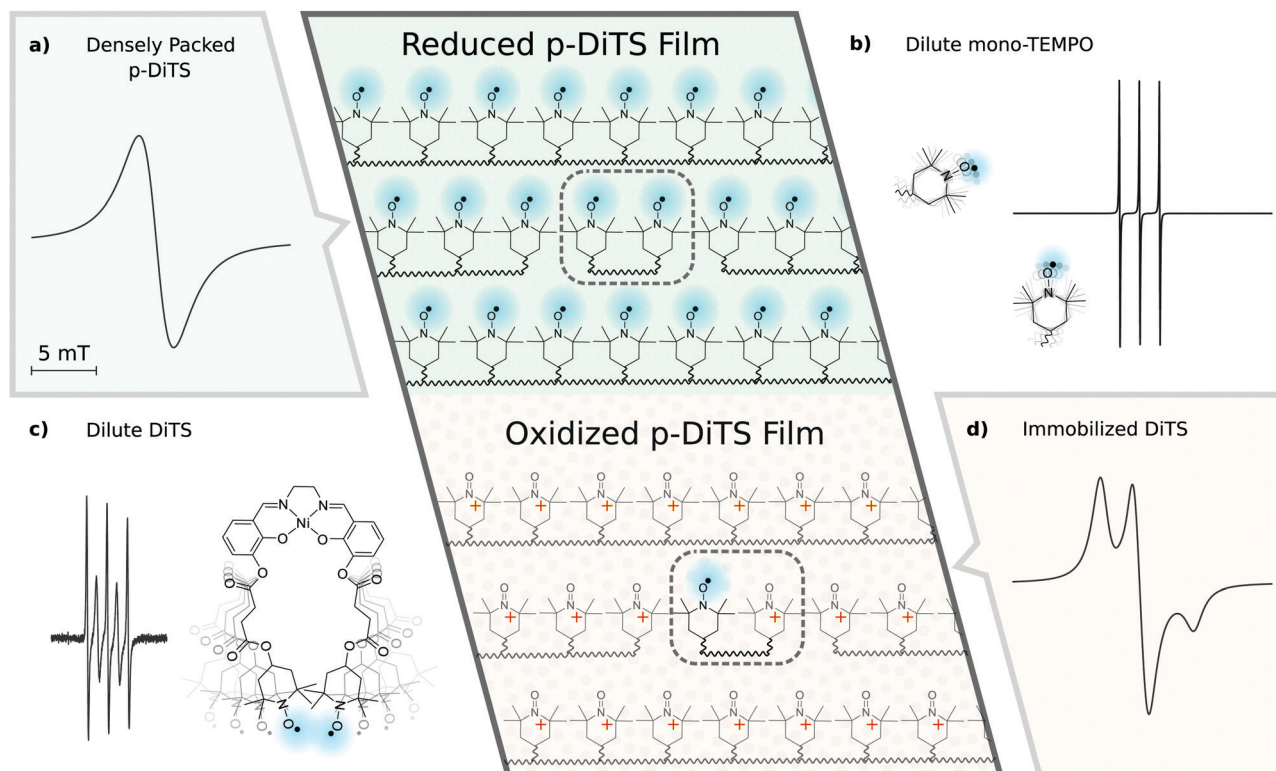


**Fig. 2** Classification of the nitroxide cwEPR spectra observed for p-DiTS under different conditions and in different environments. (a) Densely packed nitroxide film with dipolar broadening and exchange narrowing or broadening giving a single derivative line. (b) Typical spectrum of dilute mono-nitroxide in solution, three-lines due to  $S = 1/2$ ,  $I = 1$   $^{14}\text{N}$  hyperfine interaction (described by isotropic  $g$ -factor and isotropic hyperfine ( $A$ ) interaction). (c) Typical spectrum of tumbling di-nitroxide in solution where dynamic changes in the nitroxide–nitroxide distance modulate the exchange interaction yielding a five-line structure with alternating line width (measured cwEPR of DiTS monomers in solution at room temperature). (d) Immobilized nitroxide spectrum with both  $g$  and  $A$  anisotropy.





monomer contains two interacting EPR-active nitroxides. The spectrum depends on dynamic effects, specifically the modulation of the exchange interaction between both radicals of each monomer. Thus, depending on the solvent and temperature, the spectrum can be indistinguishable from the three-line spectrum of mono-TEMPO fragments.

The fully charged (oxidized) p-DiTS film can contain electrically isolated domains in which the nitroxides are not connected to the electrode and cannot be oxidized or reduced. These electrically inactive immobilized DiTS monomers in the oxidized film display a spectrum as shown in Fig. 2(d). In contrast to the densely packed p-DiTS film, the dipolar and exchange interactions between neighboring radicals are much weaker. The anisotropy of the nitroxide's hyperfine tensor adds features to the cwEPR spectrum in (d) as compared to (a). Yet, there is some remaining line broadening that does not allow one to distinguish between immobilized DiTS monomers with either one or two paramagnetic nitroxides.

We note that the oxidized NiSalen backbone can contribute to the spectrum as well. Its EPR signature, which is not shown in Fig. 2, is clearly different from the nitroxide/TEMPO-related spectra discussed above.

### 3 Results and discussion

To establish the extent to which the modified tube improves the resonator  $Q$ -factor ( $Q$ ) and therefore sensitivity of the cwEPR experiment, cwEPR spectra and associated  $Q$ -factors were recorded for a flat-electrode p-DiTS cell assembled in two different sample tubes. For both cell setups we used enough electrolyte to submerge all three electrodes. This required 100  $\mu\text{L}$  for the standard tube and 70  $\mu\text{L}$  for the modified tube. The effect of the two tubes on the cwEPR spectrum and on the  $Q$ -factor was studied for a range of heights ( $H$ ) measured from the center of the microwave resonator to the middle of the WE.

We determine  $Q \approx 7800$  for the empty resonator. Inserting the tube-based cells initially at  $H = 24$  mm reduces the  $Q$ -factor for both cases, but more significantly for the standard tube ( $Q_{\text{standard tube}} \approx 4200$ ,  $Q_{\text{modified tube}} \approx 5400$ , see Fig. 3). At  $H = 18$  mm the  $Q$ -factor drops for both, again more significantly for the standard tube to  $Q_{\text{standard tube}} \approx 300$  while for the modified tube it is still  $Q_{\text{modified tube}} \approx 1200$ , a factor of 4 difference. This difference between the two tubes shows the benefit of using the modified tube and flat electrode geometries for SEC EPR. When the modified tube is inserted as deep as  $H = 14$  mm, the  $Q_{\text{modified tube}}$  is around 400, which still allows for EPR measurements. Coupling the resonator was not possible for  $H < 18$  mm (standard tube) and  $H < 14$  mm (modified tube).

The decreasing  $Q$ -factor is not the only effect of a high-dielectric sample in an EPR resonator. The interaction between the sample and the electric field distribution of the resonator causes a mixture of absorption and dispersion signals, leading to asymmetric lineshapes in the cwEPR spectra. This makes double integration of the derivative cwEPR signal more complex,

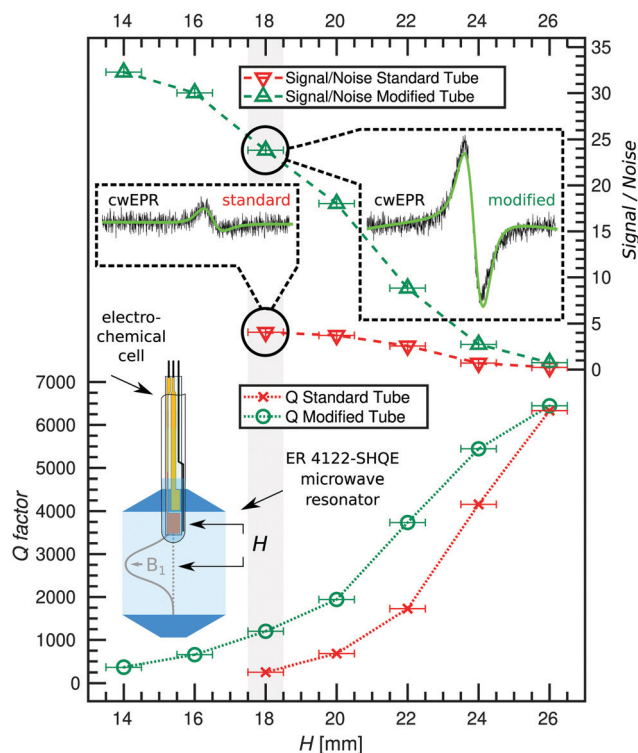


Fig. 3 Signal-to-noise ratio of the cwEPR spectrum of p-DiTS and the  $Q$ -factor of the Bruker ER4122-SHQE microwave resonator measured for an electrochemical cell based on a standard X-band EPR sample tube and for an electrochemical cell based on the modified tube. Data for various heights  $H$  from the center of the resonator. Insets: Representative cwEPR spectra at  $H = 18$  mm, where the signal for the standard tube is the strongest.

thereby making a quantitative analysis more difficult. This effect can be seen in the cwEPR spectra of p-DiTS (Fig. 3) measured in the standard 5 mm tube for  $H = 18$  mm where the cwEPR signal is asymmetric. The modified tube yields symmetric lineshapes at the same sample heights. Further details are presented in Section S2 (ESI†).

The modified tube also allows for larger cwEPR signal intensities as it can be inserted closer to the resonator center. The signal-to-noise ratio (S/N) for the modified tube is increased by a factor of  $\approx 6$  as compared to the standard tube, both inserted at  $H = 18$  mm. At the maximum sample insertion, the S/N is improved by a factor of  $\approx 8$  for the modified tube.

Using the modified tube we see three major benefits. Firstly, it results in much higher  $Q$ -factors and therefore sensitivity when comparing  $Q$ -factors for the same sample height. Secondly, the modified tube allows for insertion of the tube closer to the resonator center, allowing for a larger S/N and therefore requiring less averaging time for each cwEPR measurement. This is especially useful for samples where holding the potential for long periods causes unwanted effects or degradation. Thirdly, cwEPR measurements with the modified tube give symmetric cwEPR lineshapes (using the conventional procedure for critically coupling the microwave cavity, the standard tube gives an asymmetric lineshape) which allows



for more straightforward quantitative analysis (spin counting), especially useful for *in situ* cwEPR with varying redox potentials.

### 3.1 p-DiTS in *operando* redox series

Potential dependent *in operando* SEC cwEPR was measured on a  $40 \pm 5$  nm thick (8 deposition cycles) p-DiTS film inside the modified EPR tube at room temperature (see Fig. 4). At 0.3 V (vs. Ag) the TEMPO fragments are in the reduced/discharged state. The discharged film exhibits a single Lorentzian derivative lineshape with a peak-to-peak line width of 1.4 mT. The single-line derivative lineshape results from the collapse of the hyperfine structure due to strong exchange coupling in the films with high spin concentration, whereas the broader line width is due to a combination of dipolar and exchange coupling between the nitroxide spins within the film. In this reduced, neutral radical state the number of unpaired electrons in the film was calculated to be  $6 \times 10^{14}$  (with up to 20% error in quantitative cwEPR). This is comparable to the number of electrochemically active TEMPO charges at  $8 \times 10^{14}$ , determined by integration of the reduction branch of the CV of the cell vs. time.

Upon increasing the oxidation potential, there is no significant change in the cwEPR spectra in the oxidation potential

range between 0.3 V and  $\sim 0.8$  V (region I). A representative cwEPR spectrum from region I, taken at an oxidation potential of 0.6 V, is shown in Fig. 4(c), where the peak-to-peak line width is 1.4 mT. There is no significant change in the number of spins (spin count) contributing to the cwEPR spectra at all potentials in region I, as shown in Fig. 4(b). The cwEPR signal intensity starts to decrease at 0.8 V, and from 0.85 V to 0.94 V (the maximum potential applied to this cell), the signal intensity drops sharply. The lowest spin count is observed at an oxidation potential of 0.94 V giving  $5 \times 10^{13}$  spins. This is an order of magnitude decrease in the number of unpaired electrons in the oxidized film as compared to its initial, reduced state.

Upon closer inspection, by averaging the cwEPR spectra in the oxidized region II (between the potentials of 0.90–0.94–0.82 V), one clearly sees that the spectral shape has substantially changed from the initial region I spectrum. The region II averaged spectrum can be decomposed into two spectral components (see Fig. 2(c)) by simulating the spectra with the MATLAB toolbox EasySpin<sup>46</sup> (“garlic” function). Component 1 (“packed”) is again a broad Lorentzian derivative, similar to that of region I, but with an increased line width of 1.8 mT. Component 2 (“dilute”) is a fast-motion spectrum of tumbling nitroxides.

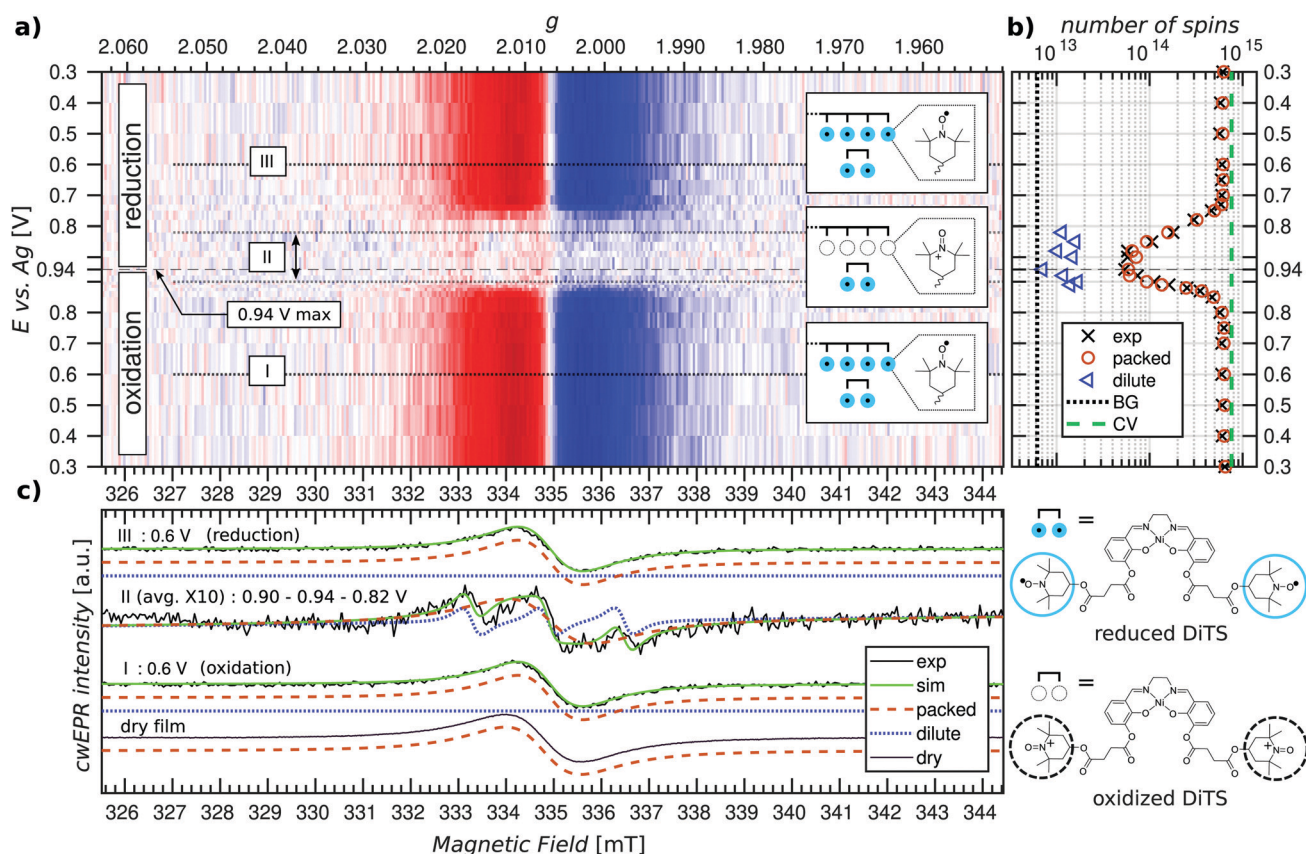


**Fig. 4** Room-temperature *in operando* cwEPR for a p-DiTS electrochemical cell. (a) CwEPR spectra during charging (oxidation) and discharging (reduction) of the cell. (b) Number of unpaired electron spins determined from a quantitative analysis of the spectra (exp). Deconvolution of the total spin count into packed and dilute spectral components. Number of electrochemically active electrons in the p-DiTS film determined from its cyclic voltammogram (CV). Background spin count on a cell without the p-DiTS film (BG). (c) Slices of subplot (a) for the initially discharged state (I, 0.6 V), charged state (II, 0.90–0.94–0.82 V, averaged within the region denoted by  $\updownarrow$ , scaled up  $\times 10$ ), and the final discharged state (III, 0.6 V). Two-component spectral simulations to identify the contributions of dilute and packed nitroxide fragments at each potential. Potentials were recorded vs. Ag RE.





The presence of component 1 even at the oxidation potential of 0.94 V is at first unexpected, as at this potential the CV curve shows full TEMPO oxidation. We therefore suggest that component 1 corresponds to local islands of still densely packed spins, which are electrically disconnected from the rest of the film (and the electrodes) and hence not redox active. The line width of component 1 in region II at 1.8 mT is slightly broader than in region I, suggesting a change in the spin-spin couplings. Looking at the line width of component 1 at different oxidation and reduction potentials (*cf.* Fig. S4, ESI<sup>†</sup>), we clearly see a trend in that the line width increases from  $\approx 1.3$ –1.4 mT in the beginning of region I to  $\approx 1.8$  mT by the end of region I, at 0.9 V. The reverse is true for region III, where the line width decreases from  $\approx 1.8$  mT at 0.9 V back to  $\approx 1.3$ –1.4 mT at 0.3 V. Since the dipolar coupling between the spins should only decrease with increasing potentials (reducing spin count in the film) resulting in a decreasing line width, we expect the observed line width behavior (increasing line width when going from 0.3 V to 0.9 V) to be due to decreasing exchange coupling. As the film is oxidized, the spin density in it decreases. That reduces the exchange coupling between neighboring spins, which transforms an exchange narrowed spectrum (strong exchange coupling) into an exchange broadened spectrum (weaker exchange coupling). However, the spin concentration in the film cannot be decreased to a point where the hyperfine structure can be resolved.

Furthermore, since the component 1 spectra in region II are likely to be due to local islands of electrochemically inactive charged species, their spectral line width depends on the local spin concentration before the charges/islands become electrically inactive. It is unclear why the line width observed for component 1 is larger in region II, though possible reasons are weak cwEPR signals introduce a systematic error into the two-component spectral deconvolution, or the exchange narrowing effect is less pronounced at the decreased spin concentration, or there is a changing morphology during oxidation. The idea of electrically disconnected islands or domains will be further explored later on in this article.

The presence of component 2 (three-line feature described by an isotropic *g*-factor and hyperfine interaction) is, as discussed in Section 2.3, due to mobile nitroxide spins. The presence of a three-line component but no detectable five-line component suggests the nitroxide spins in electrolyte are not due to the release of monomers (as expected for this film because it underwent the cleaning procedure described in Section 2.2 to remove any non-polymerized DiTS). The three-line feature must therefore be due to molecular breakdown of DiTS to release mono-nitroxide fragments in the electrolyte.

We determine the spin counts for the components 1 and 2 by double integration of the simulation traces around 0.94 V. Component 1, the packed immobilized nitroxide spins, corresponds to a spin count of  $4.8 \times 10^{13}$  at 0.94 V (Fig. 4(b), orange circles), while component 2, the dilute mobile nitroxide spins in electrolyte, corresponds to  $\approx 1 \times 10^{13}$  (Fig. 4(b), blue triangles). The number of spins due to nitroxide groups dissolved in the electrolyte is only  $\sim 1.6\%$  of the total spins in the

initial film (*cf.* total initial spin count of  $6.4 \times 10^{14}$ ). The number of nitroxide spins, which are still part of the film but not oxidized, is only  $\sim 7.5\%$  of the initial spin count. This shows that over 90% of the p-DiTS film is electrochemically active.

Looking at the oxidation series from 0.3 V to 0.94 V and the reduction series from 0.94 V back to 0.3 V, we see that the reduction occurs over a larger potential range as compared to the oxidation (*cf.* Fig. 4(b)). This suggests a changing morphology of the p-DiTS film upon oxidation, which decreases electrolyte access to the TEMPO groups in the film matrix. A similar trend is seen in thicker films, where again oxidation occurs over a narrower potential range than reduction (see Fig. S6, ESI<sup>†</sup>). This is a known phenomenon whereby, during oxidation, the pores and channels in the polymer film open and counter ions from the electrolyte enter the film matrix, aiding the oxidation process. During reduction, the opposite is true whereby the polymer film shrinks, and hence expulsion of counter ions slows down as a function of time. This results in a broadening of the left-hand side of the reduction branch in a CV and a slower recovery of the TEMPO spin count during the reduction series in quantitative *in operando* cwEPR.

While the EPR signatures of different polymeric NiSalen complexes have been reported by Dmitrieva *et al.*,<sup>43</sup> we do not observe the EPR signature of the NiSalen backbone in our *in operando* study of p-DiTS. Dmitrieva *et al.* noted that upon increased doping of the polymer (still one hole per monomer unit), the charges could aggregate to form diamagnetic states, and under high oxidation potentials the polymer could be doped with two holes per monomer, thus also forming diamagnetic dications. Another plausible explanation for the absence of a p-NiSalen EPR signal could be related to low-intensity signals which are masked by the much more intense nitroxide signals. However, our quantitative EPR analysis of the number of spins per monomer unit in the p-DiTS film gave  $2.0 \pm 0.2$ , suggesting only signals corresponding to nitroxide radicals, as there are two unpaired nitroxides per DiTS monomer unit: in its charge-bearing groups. In addition, Coulomb repulsion between the positively charged TEMPO<sup>+</sup> groups in the oxidized state and the positive polarons on the backbone could lead to a depletion of mobile positive charge carriers and thus provide a credible explanation for the absence of a corresponding polaron EPR signal.

### 3.2 cwEPR – a tool to determine the quality of ORB polymer films

An important parameter for designing a battery system is the purity of the active layers (cathode and anode). CwEPR can play a vital role in investigating the purity of the active polymer layer in ORBs by distinguishing between molecules which are redox active and contribute to the capacity and those that are not. Furthermore, cwEPR can be used to identify the contributing and non-contributing molecules by changes in spectral signature, based upon which improvements can be made to battery or active layer materials.



**3.2.1 Release of nitroxide fragments into electrolyte.** During the electropolymerization process it is possible that some non-polymerized monomeric DiTS gets trapped in the pores or inter-layer structure of the growing polymer film. These monomers are likely not redox active as they are not directly linked *via* a long conductive backbone to the rest of the film and to the electrodes. More crucially, however, these monomer units could be released into the liquid electrolyte, where they serve as redox shuttles that cause self discharge of the cell, while the self-discharge rate depends on the concentration of the redox shuttles in the electrolyte. Side reactions between the film and the electrolyte can additionally contribute to self discharge. However, since the contamination level in the battery-grade electrolyte is very low, and we are working in a potential window in which the electrolyte is stable, we assume that the main contribution to the self-discharge rate is caused by redox shuttles. The self-discharge effect may be similar to an internal short-circuit at high redox-shuttle concentrations. To investigate the release process, we measured the *in operando* SEC cwEPR of a 150 CV cycle ( $t = 400 \pm 40$  nm) p-DiTS film, which had not gone through the rinsing procedure, *i.e.* contained monomeric DiTS. For an electrochemical cell based on such a film, the dominant spectral signature is of monomeric DiTS, for both reduced and oxidized states (see Fig. S5, ESI†). The monomeric DiTS yields a characteristic five-line structure as described in Section 2.3. For such a film, both *in operando* cwEPR spectra and the spectra of the rest electrolyte show the five-line monomeric DiTS spectra, confirming release of monomers into the electrolyte (primary release).

After the primary release of monomeric DiTS from the film, the film is not expected to show any DiTS monomer spectra. However, to be certain that the monomers are removed, the p-DiTS film was further rinsed in ACN, and the electrolyte was replaced before carrying out a further *in operando* study on this sample.

In the second *in operando* SEC cwEPR study (Fig. 5(a)), the cwEPR spectra at 0.3 V show single Lorentzian derivative lineshapes corresponding to the exchange/dipolar coupled densely packed nitroxide spins, with a line width of 1.7 mT. Upon oxidizing the film to 0.9 V, the cwEPR signal intensity decreases by a relatively small amount. However, at 1.1/1.2 V the packed component disappears and we see the full oxidation of the film. The residual signal in the 1.1/1.2 V cwEPR spectrum is a three-line spectrum, which indicates that there are mono-TEMPO fragments dissolved in the electrolyte. The presence of mono-TEMPO in the electrolyte (also confirmed by measuring the rest electrolyte) suggests degradation of the DiTS monomers. This degradation and the release of nitroxide fragments into the electrolyte hinders the performance of ORBs as the released fragments not only decrease the electrical capacity, but can also discharge the battery by acting as redox shuttles between WE and CE. As can be seen from the reduction steps between 1.1 V and 0.3 V, the one-line spectral feature recovers, but not to the same initial intensity, and the increasing three-line component is seen superimposed.

While electrochemical quartz crystal microbalance measurements can hint towards loosely bound oligomers or trapped

monomers being released from a newly grown polymer film after rinsing or initial CV cycling, it cannot distinguish between (1) oligomers and monomers released and (2), as relevant for DiTS, between mono-TEMPO fragments and di-TEMPO monomer units. CwEPR can give information in both of the mentioned cases, for (1) through changes in rotational correlation time ( $\tau_c$ ) between monomers (short  $\tau_c$ ) and oligomers (long  $\tau_c$ ) due to an increasing molecular size and for (2) changes from three-lines to five-lines spectra due to dynamic exchange coupling which is present in the di-TEMPO monomer but not in the mono-TEMPO fragments.

Further investigation of this three-line feature could lead to information about the size of the fragments by comparison to three reference samples, namely TEMPOL, the mono-TEMPO succinyl moiety, and mono-TEMPO NiSalen in electrolyte solution and studying their rotational correlation times. The exact size and nature of the nitroxide fragments is beyond the scope of the current study but it can be identified with EPR.

**3.2.2 Re-polymerization and missing spins.** In a  $500 \pm 60$  nm thick p-DiTS film which was made using 200 CV cycles and underwent the rinsing procedure mentioned before, the cwEPR signal of the fully reduced state (0.3 V vs. Ag, Fig. 5(b)) shows a significant increase in the signal intensity due to the increased thickness and it being the first *in operando* study on this film. Upon applying an oxidation potential of 0.9 V, the one-line broad feature (1.3 mT line width) decreases as is expected for the oxidation of the p-DiTS film. At the same time, three satellite peaks emerge, corresponding to mobile nitroxides. After further oxidation to 1.1 V, the one-line feature disappears, which corresponds to the full oxidation of the film. A three-line spectrum is still present, though even less intense than can be observed in the 0.9 V oxidation spectrum.

Reducing the film back from 1.1 V to 0.9 V, we see the partial recovery of the signal, and similarly reducing back to 0.3 V still only results in partial reduction of the film/recovery of the cwEPR signal. Since it is well known that TEMPO exhibits a reversible redox reaction between  $\text{TEMPO}^\bullet \rightleftharpoons \text{TEMPO}^+$ , it is unlikely that the decrease in overall signal intensity in Fig. 5(b) during the full redox cycle is due to a chemical reaction. Rather the more plausible explanation is that oligomers in this thick film are oxidized and then detach from the electrode, thereby no longer being electrically accessible for reduction and also not appearing in the only electrolyte spectrum as  $\text{TEMPO}^+$  is EPR silent. Furthermore, the presence of satellite peaks corresponding to mobile nitroxides is different to the case seen in Fig. 5(a). The presence of a superimposed three-line spectrum (Fig. 5(b), 0.9 V oxidation, dotted blue curve), which can be electrochemically oxidized and does not reappear in the 0.3 V reduction spectrum, suggests that this signal corresponds to oligomers which are electrically connected to the electrode but are initially mobile. Such behavior could be expected of oligomers near the film surface, where one end can be mobile and the other end is connected through the main film structure to the electrodes. After initial oxidation up to 1.1 V, the mobile end of the oligomer either goes through a polymerization reaction, whereby it becomes more rigidly connected to the





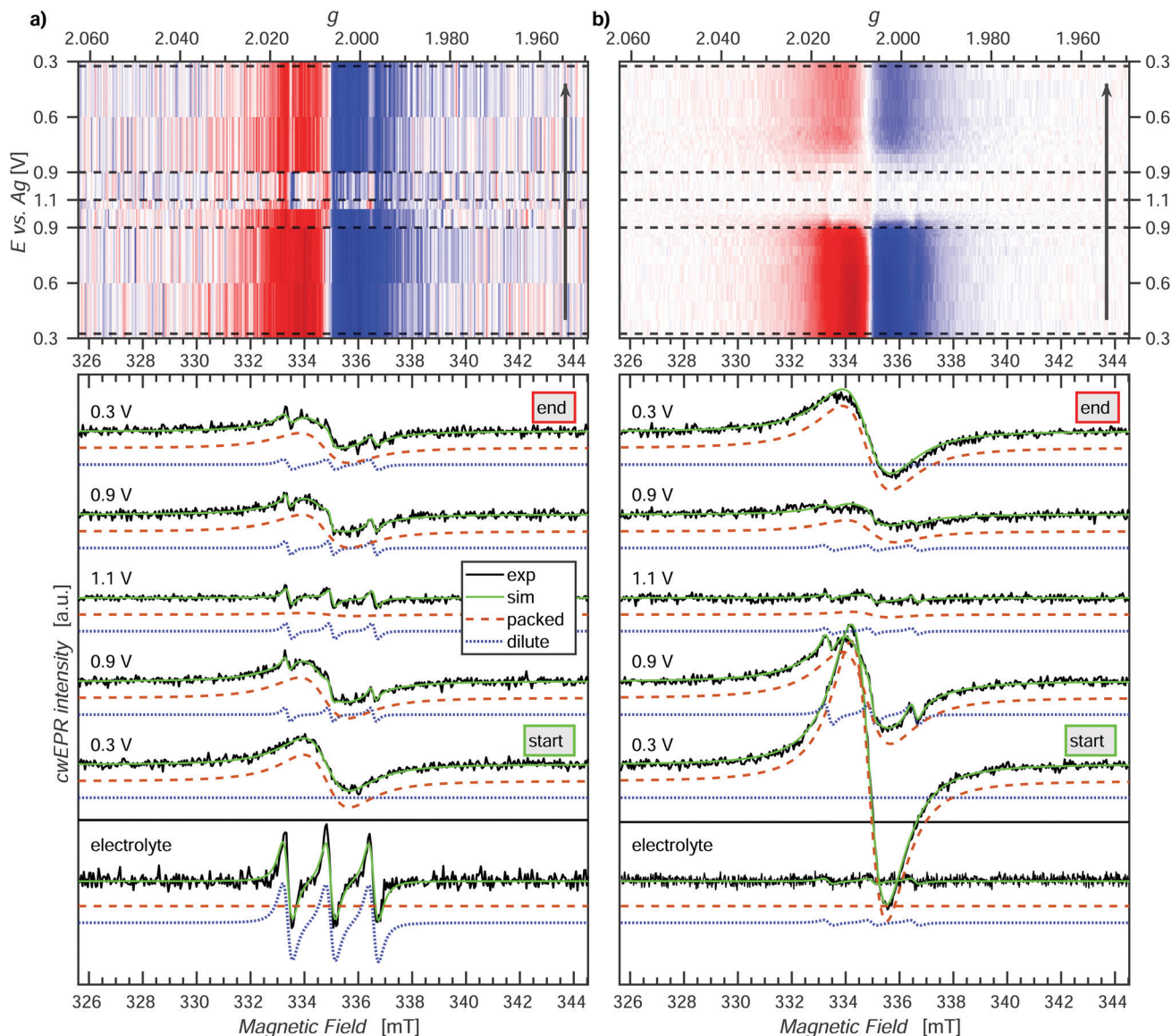


**Fig. 5** Room-temperature *in operando* cwEPR measurements for two p-DiTS electrochemical cells. Two-component spectral deconvolution to identify dilute and packed nitroxide fragments. Spectra of the rest electrolyte for both cells. (a) Cell with a p-DiTS film grown by 150 deposition cycles ( $t \approx 400$  nm) that was left untreated and underwent one charge–discharge cycle before the measurement. The dilute component is released during the oxidation and remains detectable in the rest electrolyte. (b) Cell with a p-DiTS film grown by 200 deposition cycles ( $t \approx 500$  nm) that was rinsed in solvents and cycled in the electrolyte to remove the not polymerized nitroxide fragments. The initially released dilute component is electrochemically active.

film, or, possibly, the oxidized oligomers get released to the electrolyte, where they stay in the oxidized, EPR-silent state.

The spectral deconvolution into the components 1 (packed exchange/dipolar coupled spins) and 2 (dilute mobile spins) together with the evolution of the spectral shape and line width is presented in Fig. S6 (ESI<sup>†</sup>).

SEC cwEPR offers a powerful tool to understand differences in film behavior with different thicknesses and changes in the local film structure. The above study shows three different yet important pieces of information that SEC cwEPR can yield, which are not readily available from conventional electrochemistry techniques. Firstly, SEC cwEPR can not only detect/quantify that

some active electrode material is lost to the electrolyte, but also indicate if the released material is in an oxidized or reduced state. This information is not available from electrochemical techniques alone, as the released fragments may not be electrochemically active. Secondly, it was observed through clear spectral signatures that some nitroxide pendant groups in the electrochemical cell are mobile yet still electrochemically active. Thirdly, through changes in the intensity of the dilute component and the line width of the broad spectral component one can observe how these initially mobile groups subsequently become immobilized (and/or oxidized) as the oligomer backbone (re-)polymerizes to the main film structure. Such subtle differences in film structure



and behavior during operation are vital for understanding and improving organic materials for active electrode materials in ORBs. In addition, SEC cwEPR can potentially also be employed to study the film growth during electropolymerization. This powerful spectroelectrochemical tool may be used to assist not only synthetic- and electro-chemists but the ORB field in general.

### 3.3 Degradation of p-DiTS upon charge–discharge cycling

ORBs based on p-DiTS were shown to lose their capacity under repeated charge–discharge cycling,<sup>31</sup> but the mechanism of degradation is not yet understood on the molecular level. In order to study the processes occurring during degradation, we recorded CV curves along with cwEPR spectra during charge–discharge cycling of a tube-based p-DiTS electrochemical cell.

For this purpose, a  $400 \pm 50$  nm thick p-DiTS film (Fig. S3(d), ESI†) was deposited onto the on-substrate WE. The cell was inserted into the microwave resonator of the cwEPR spectrometer at  $H \approx 14$  mm where it underwent a series of 36 charge–discharge cycles at a rate of  $5 \text{ mV s}^{-1}$ . The CV curves were recorded for each cycle. The cwEPR spectra were recorded after each fourth cycle for the fully reduced/discharged cell, that is at the left-most point on the corresponding CV.

Fig. 6 shows the cwEPR spectra (a) and the CV curves (c) measured during the repeated cycling of the electrochemical cell. During the cycling, the CV curves decrease in intensity, indicating a decrease in the number of the electrochemically active charges in the film. The number of electrochemically

active charges was determined for each cycle by integrating the reduction branch of the corresponding CV. It is plotted together with the quantitative EPR results, labeled as “CV” in Fig. 6(b). The spectra, CV and quantitative analysis for the intermediate cycles are shown in Fig. S7 (ESI†).

The cwEPR spectra in Fig. 6(a) demonstrate an initial release of the dilute component and a decrease in intensity upon further cycling. The three-line dilute component corresponds to TEMPO• fragments that detach from the film in the reduced state and get released to the electrolyte. The dilute component is emerging only during the first eight cycles. Meanwhile, the magnitude of the CV (*cf.* Fig. 6(c)) stays as high as  $100 \mu\text{A}$  during the first eight cycles. This suggests that the initial release of the reduced, EPR-active TEMPO fragments does not significantly affect the capacity of the cell and can be excluded as the main degradation pathway.

The broad, single-line packed component, on the contrary, keeps decreasing for  $>8$  cycles, together with the CV. Therefore, the degradation of the electrical capacity of the p-DiTS film has to be associated with the decrease in the signal intensity of the packed component and is not accompanied by the release of any EPR-active products to the electrolyte.

The number of paramagnetic states in the film after each degradation step, as determined by a quantitative analysis of the respective spectral components, is shown in Fig. 6(b) along with the number of electrically active charge carriers. For the fresh film (“0 CV”), the quantitative EPR and CV results are in good agreement. In contrast, there is a significant difference

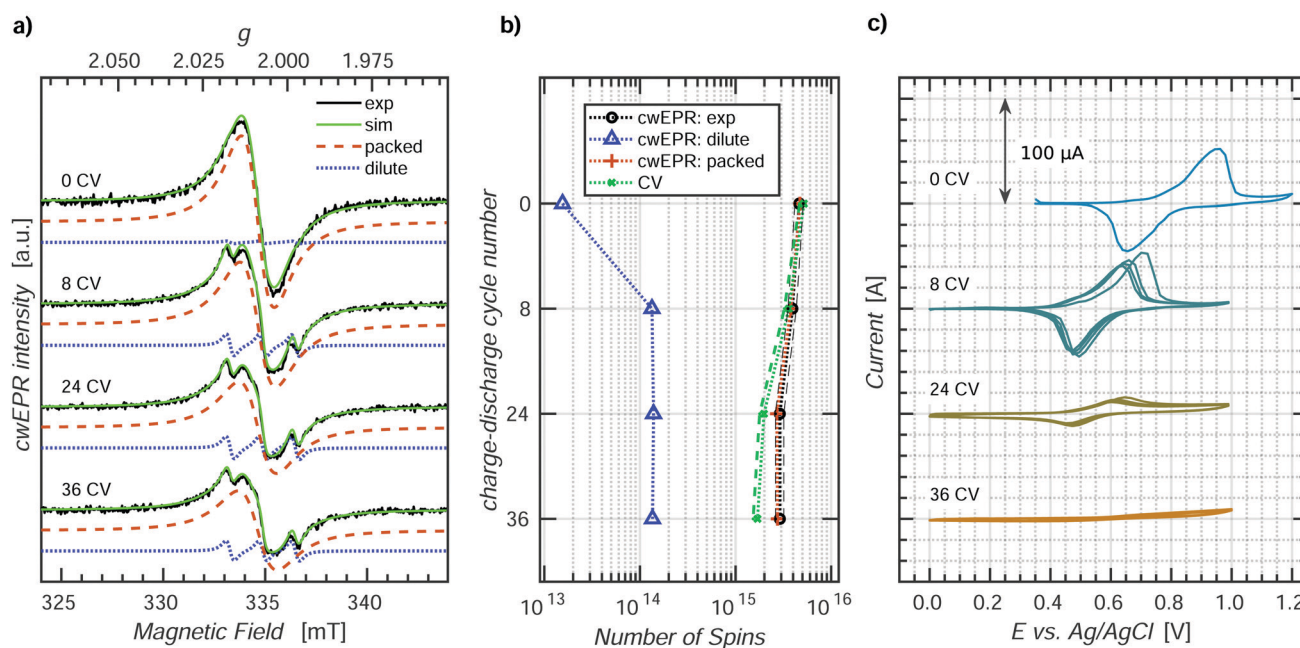


**Fig. 6** (a) Room-temperature cwEPR spectra for a p-DiTS electrochemical cell with a  $\approx 400$  nm thick p-DiTS film cathode undergoing 36 charge–discharge cycles and exhibiting degradation of electrical capacity. Two-component spectral deconvolution to identify dilute and packed nitroxide fragments. (b) Spin count of the separated cwEPR spectral components and the number of electrochemically active charges extracted from the CV curves at the corresponding charge–discharge cycle. (c) Cyclic voltammograms of the cell, representing the charge–discharge cycles. The voltammograms were recorded with respect to Ag/AgCl RE at a rate of  $5 \text{ mV s}^{-1}$  in the modified tube inside the microwave resonator, inbetween the cwEPR scans.





after 36 cycles. This experimental observation can be rationalized as follows.

All cwEPR spectra in Fig. 6(a) were recorded when the film was brought to the reduced state, with all electrochemically active TEMPO<sup>•</sup> fragments being also EPR active. Additionally, all electrochemically inactive fragments that happen to be in the reduced, TEMPO<sup>•</sup> state also contribute to the cwEPR signal. Thus, the cwEPR signal after each charge–discharge cycle contains contributions from electrochemically active and electrochemically inactive TEMPO<sup>•</sup> fragments, and both components contribute to the overall number of spins shown in Fig. 6(b).

The intensity of the packed spectral component substantially decreases with cycling. This indicates that some paramagnetic parts of the film (TEMPO<sup>•</sup>) become diamagnetic (TEMPO<sup>+</sup>) and stay EPR silent when the cell is brought back to the reduced state. These fragments may either stay in the film or are released into the electrolyte. As a previous study reported no loss of mass of a p-DiTS film in a microbalance-monitored charge–discharge cycling,<sup>31</sup> we assume that the oxidized and electrically disconnected, EPR silent fragments do not leave the film.

Upon cycling, the number of electrochemically active charged species decreases stronger than the number of paramagnetic states (Fig. 6(b)). This indicates that some regions of the film become redox inactive upon cycling but still contribute to the EPR spectrum. These TEMPO<sup>•</sup> fragments lose the electrical connection to the rest of the film (and thus to the metal electrode) and stay in the reduced state. The possible degradation of a p-DiTS film leads to the interruption of a conductivity pathway, resulting in the formation of electrically isolated domains within the film. We suggest that these isolated domains are also responsible for the remaining packed EPR signals observed for the nominally fully-oxidized film in the *in operando* redox measurement (Fig. 4).

### 3.4 Low-temperature *ex situ* SEC cwEPR

While *in operando* SEC cwEPR provides information about redox systems in their natural operating environment, these measurements are limited by the time for which potentials can be applied before degradation of the active materials is observed. In contrast, in *ex situ* experiments on cells without electrolyte, the desired redox states of the films can be observed for longer times without degradation effects. Additionally, *ex situ* measurements can be performed at cryogenic temperatures, which drastically increases the EPR signal intensity.

**3.4.1 p-DiTS.** For the p-DiTS cells, *in operando* SEC cwEPR measurements were carried out at room temperature while holding the cell at redox potentials of interest for ~200 seconds during the accumulation of the cwEPR spectra. The S/N for this setup is limited by the time available to acquire EPR spectra and by the low spin polarization at room temperature. We therefore perform *ex situ* measurements on a 95 deposition cycle ( $t = 400 \pm 40$  nm) film at cryogenic temperatures, in this case at 150 K. These *ex situ* measurements involved bringing the cell to the chosen redox potential using the setup shown in Fig. 1(c), outside the spectrometer. The potential was applied for 100–200 seconds.

Then the electrodes were disconnected from the cell. Subsequently, the substrate with the on-substrate electrodes was placed in a standard 5 mm OD quartz tube filled with N<sub>2</sub> gas and sealed using a septum and Parafilm to prevent condensation of water in the tube. This method can hold the cell in different redox state regions but not necessarily the exact set redox potentials, as the charge seems to equilibrate to different overall states. This was determined by comparison of our *ex situ* cwEPR results and spectral simulations to *in situ* spectra shown in ref. 43. The aim of the *ex situ* measurement was to reach representative redox states which were also seen in the *in operando* measurements (Fig. 4), *i.e.* fully reduced, partially oxidized and fully oxidized states, with a higher S/N.

We therefore measure the *ex situ* SEC cwEPR at different oxidation potentials, three of which are shown in Fig. 7(a). At 0.1 V the p-DiTS film is in the reduced state and exhibits a one-line feature corresponding to densely packed spins. At 0.6 V and 0.9 V the overall signal decreases significantly and a similarly broad yet distinctly different signal appears. The signal at each of the three potentials has contributions from the nitroxides/TEMPO groups in two distinctly different environments. The broad one-line feature arising from densely packed dipolar and exchange coupled nitroxide spins, and dilute immobilized nitroxide spins, described by a rhombic *g*-tensor. We can simulate the measured spectra at each oxidation potential using EasySpin<sup>46</sup> (“pepper” function), assuming a combination of packed and dilute contributions with changing relative weights. We find that with increasing oxidation potential the one-line packed nitroxide feature decreases, but the intensity of the dilute immobilized nitroxide does not change. The film in this *ex situ* study did not contain any electrolyte, so both spectral components correspond to the nitroxide spins in the film. The spins may be situated either on mono-TEMPO fragments or di-TEMPO DiTS, but with the nitroxide groups situated far apart, resulting in a small exchange coupling and hence three instead of five lines in the spectrum. This suggests that the p-DiTS films have some nitroxide spins which are not electrochemically active yet are still a part of the film structure, again suggesting domains of electrochemically inactive spins – except this time in the paramagnetic state.

**3.4.2 p-NiMeOSalen.** During the *in operando* and *ex situ* SEC cwEPR measurements of p-DiTS (*cf.* Fig. 4 and Fig. 7(a)), we observed no signals associated with polarons on the NiSalen backbone. In contrast, Dmitrieva *et al.* have shown that polymeric NiSalen films are redox active and indeed exhibit EPR signals during *in situ* SEC cwEPR measurements.<sup>43</sup> In order to examine whether we can detect EPR signals from polarons on the backbone, we measured SEC cwEPR of p-NiMeOSalen, which closely resembles the core backbone structure of p-DiTS but does not contain any TEMPO pendant groups.

The cwEPR spectra recorded at 150 K are shown in Fig. 7(b) for a few key potentials, while the full data set is shown in Fig. S9 (ESI<sup>†</sup>). We observe clear EPR signals that can be attributed to different paramagnetic species on the polymer backbone with the weights of the individual spectral components strongly depending on the applied potential. Simulations for



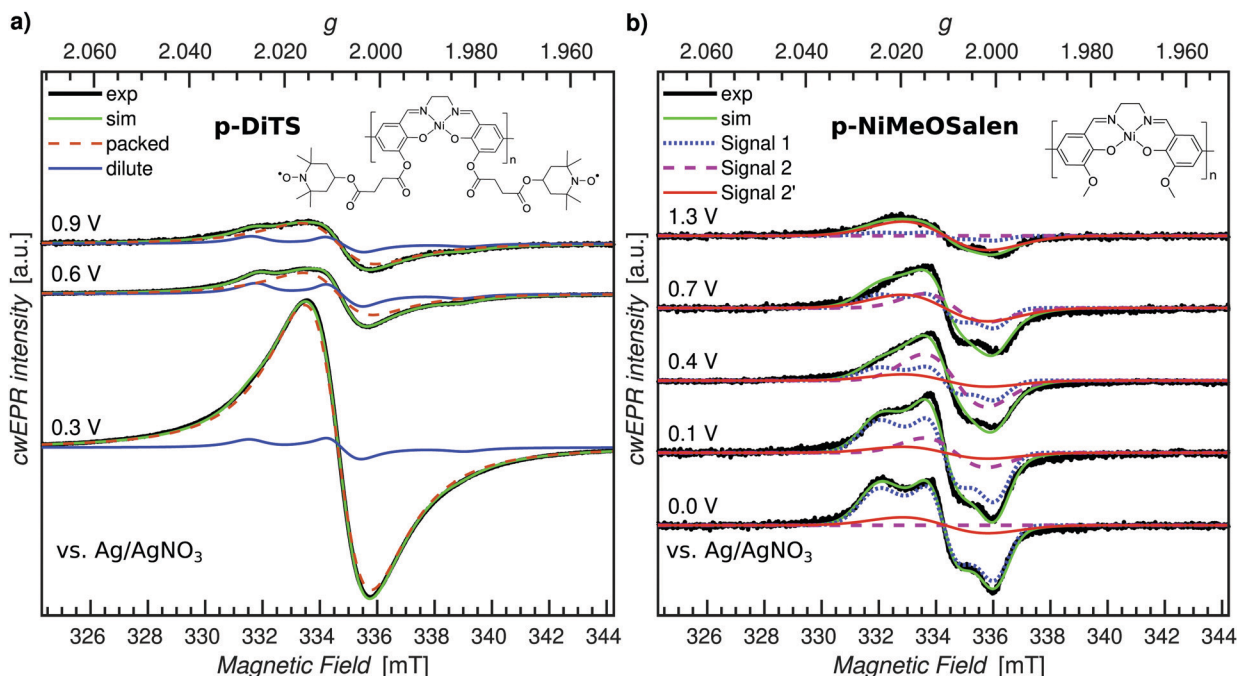


Fig. 7 Cryogenic (150 K) *ex situ* cwEPR in a range of redox potentials for p-DiTS and its molecular backbone, p-NiMeOSalen. (a) p-DiTS film ( $t \approx 400$  nm). Two-component spectral deconvolution to identify the densely packed (dashed-red curve) and dilute (solid-blue curve), immobilized nitroxide fragments. (b) p-NiMeOSalen film ( $t \approx 900$  nm). Three-component spectral deconvolution into the components observed earlier.<sup>43</sup>

three EPR-active species consistent with those reported in ref. 43 (denoted by “Signal 1”, “Signal 2” and “Signal 2’”) are shown along with the measured spectra. Details about the change in the EPR signal as a function of the oxidation potential as well as the spectral simulations can be found in Section S7 (ESI†).

Based on the p-DiTS and p-NiMeOSalen *ex situ* studies it is clear that both the TEMPO and NiSalen backbone are redox active, as expected. However, we neither see backbone-related EPR signals in the room-temperature *in operando* measurement (Section 3.1) nor in the low-temperature *ex situ* experiment (Fig. 7(a)) performed on p-DiTS films. The reason for the absence of a clear NiSalen signal in p-DiTS is possibly related to the formation of diamagnetic species or the depletion of polarons on the backbone due to Coulomb repulsion as mentioned before.

### 3.5 Pulse EPR on p-DiTS – a step closer to SEC pEPR

While it is highly desirable to perform *in situ* cwEPR experiments on electrochemical cells and fully processed batteries under ambient conditions at room temperature, most pulse EPR measurements performed on battery-relevant materials require low temperatures, primarily to increase spin-relaxation times. The necessity for low-temperature measurements already precludes the use of conventional flat cells in combination with cylindrical resonators.<sup>39,47</sup>

Recently, successful pEPR measurements performed on batteries based on inorganic, lithium-containing electrode materials in an X-band dielectric ring resonator were reported,<sup>27</sup> clearly

showing that pEPR experiments are indeed feasible and can provide insights into the kinetics of processes occurring on the electrodes upon fast charging. However, the cell geometry used in ref. 27 only allows for room-temperature measurements. We believe that the possibility of performing low-temperature pEPR measurements is the key to a widespread use of pEPR techniques for polymer battery research, providing access to the full arsenal of advanced echo-detected pEPR experiments. Our versatile on-substrate electrode setup (see Section 2) readily allows for low-temperature pEPR experiments.

As a first step, we sought to perform pEPR measurements on an oxidized p-DiTS film in order to detect electrochemically inactive nitroxide radicals. For this purpose, a p-DiTS cell was brought into its fully charged state at 900 mV *vs.* Ag/AgNO<sub>3</sub> and kept at this potential while the electrolyte was removed and the sample was thoroughly dried. The substrate was subsequently flame-sealed in a helium-filled quartz tube. The cwEPR spectrum measured at  $T = 80$  K (Fig. 8(a)) is indicative of immobilized, isolated nitroxides<sup>30</sup> and clearly deviates from the broad and unstructured single-line spectrum observed for a reduced p-DiTS film at room temperature (Fig. 4(c)) and at  $T = 150$  K (Fig. 7(a)). This confirms that the charge state of the p-DiTS film is indeed preserved in the electrically disconnected sample without electrolyte.

Next, we performed low-temperature pEPR measurements using the standard Hahn echo sequence ( $\frac{\pi}{2}-\tau-\pi-\tau-\text{echo}$ ). The resulting echo-detected field-sweep spectrum is shown in Fig. 8(a) along with the cwEPR spectrum measured under identical conditions. Based on the overall shape and width of



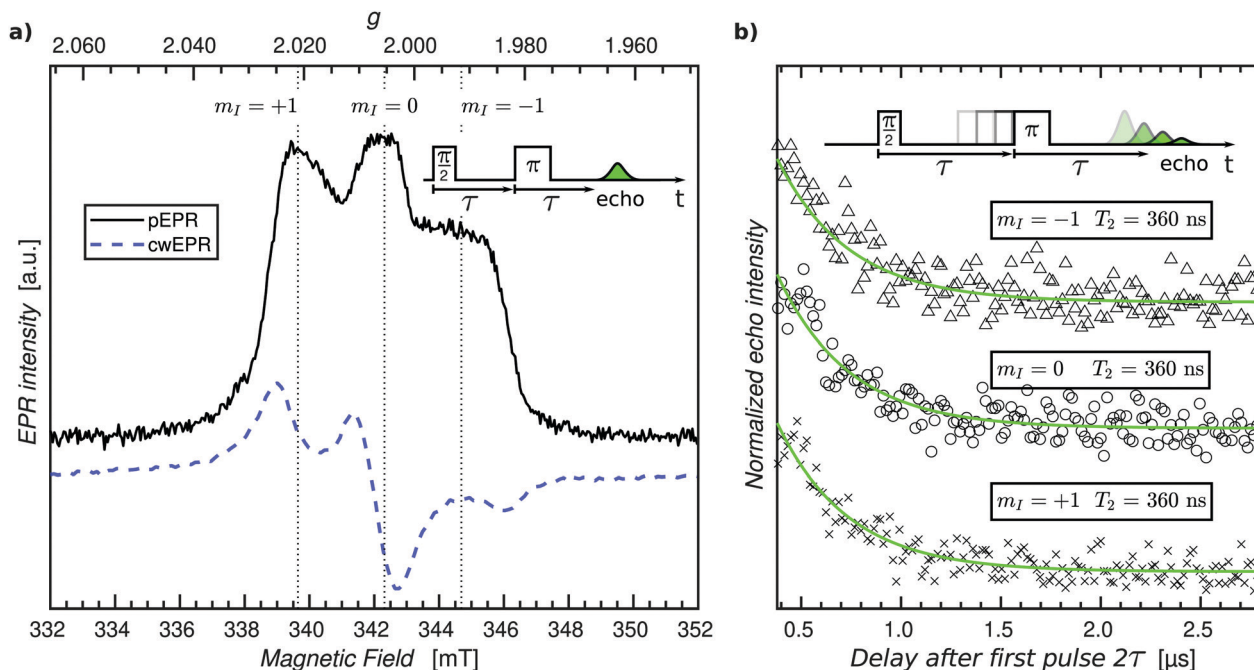


Fig. 8 (a) Pulse EPR echo-detected field-sweep spectrum (solid line) and cwEPR spectrum (dashed line) of a  $\approx 500$  nm thick p-DiTS film charged to +900 mV vs. Ag/AgNO<sub>3</sub> measured at  $T = 80$  K ( $\nu = 9.6$  GHz). (b) Results of echo-decay measurements performed at the peak positions indicated by the dotted vertical lines in (a) along with single exponential fits to determine the spin-spin relaxation times  $T_2$ .

the spectrum, which is given by  $2A_{zz}$  with  $A_{zz}$  being the  $z$  component of the hyperfine tensor, we can unambiguously attribute the resonant signal to immobilized nitroxides. However, the pEPR spectrum differs from the usual TEMPO powder spectrum. Most notably, the relative intensity of the central ( $m_I = 0$ ) peak is significantly lower than expected. Echo-decay measurements reveal that the spin-spin relaxation times  $T_2$  (Fig. 8(b)) are comparable for all three  $m_I$  components, suggesting that anisotropic relaxation is not the main reason for the reduced intensity of the central peak. On the other hand,  $T_2$  is at least one order of magnitude shorter than for isolated nitroxides, indicating that spin-spin coupling significantly influences  $T_2$  for the paramagnetic centers in the oxidized p-DiTS film.

Further measurements will help identifying the main factors responsible for the peculiar shape of the pEPR spectrum, among them possible partial ordering of the TEMPO groups in the p-DiTS film, (restricted) motion of the nitroxides even at low temperatures and/or the existence of redox-inactive sites in different microscopic environments associated with dissimilar relaxation properties.

The pEPR spectrum in Fig. 8(a) is likely a result of the same electrochemically inactive dilute spins observed in the *ex situ* p-DiTS redox series (Fig. 7(a)). Potential dependent SEC pEPR measurements are ongoing to confirm this hypothesis, and ELDOR and hyperfine spectroscopy could lead to critical information about the local environment which causes these spins to be electrochemically inactive. These advanced pEPR methods could further give insight into degradation mechanisms in p-DiTS and other ORB materials. Pulse EPR measurements on

electrochemical cells that are flash-frozen right after performing CV experiments at room temperature can potentially help to learn about the relevance of the states probed by pEPR for the device function. Realization of SEC pEPR, particularly on film electrodes, makes these techniques available for other research fields such as the study of hydrogenases and enzymes or metal catalysis.

## 4 Experimental section

See ESI.†

## 5 Conclusion and perspectives

Our results show that electron spins can be used as unique local probes for elucidating redox reactions associated with charging and discharging of ORBs with active electrode materials prepared by electropolymerization. EPR spectroscopy can thus be employed to analyze these processes, identify performance-limiting loss mechanisms, and eventually help developing strategies for making polymer batteries powerful contenders on the path towards sustainable electrochemical power sources.

The fact that we can observe a strong influence of the electrical potential on the *in situ* EPR spectrum at ambient conditions provides the basis for systematically studying the redox-active sites in different states of the active electrode materials. For instance, changes in the film structure, *e.g.* caused by degradation, can be detected in *in situ* cwEPR experiments (*cf.* Fig. 5) as nitroxides in different environments are associated with characteristic and unique EPR signatures (*cf.* Fig. 2).





Much more detailed and specific information about degradation processes can, however, be extracted from advanced (pulse) EPR experiments which usually require low temperatures, mostly to increase spin-relaxation times. We believe that the possibility of performing low-temperature pEPR measurements is the key factor that is mandatory for a widespread use of advanced EPR techniques for ORB research.

The electrochemical cells for *in situ* studies, as described in this article, were designed in such a way that they fit into a standard EPR tube. They are thus compatible with (low-temperature) experiments using conventional pEPR instrumentation. This opens up the intriguing perspective of exploiting the coupling between neighboring electron spins as well as the hyperfine coupling between electron and nuclear spins in close vicinity to determine the coupling (and thus the distance) between redox-active centers and the degree of delocalization for charge carriers on the conjugated polymer backbone. In particular, it is conceivable to find out whether inactive redox centers, which are not changing their redox state upon charging and discharging, can be found in clusters or are rather isotropically distributed in the cathode films. This provides the possibility to identify inactive redox sites that reduce the maximum attainable cell capacity. Most notably, this knowledge can be used to change the conditions during electropolymerization and thus optimize the film growth and eventually improve the electrode material performance. The pEPR measurements can either be performed *ex situ* (without electrolyte, cf. Fig. 7 and 8) or on samples that are flash-frozen while the desired electrical potential is applied to the cell.

The experiments presented here are by no means limited to the electrochemical cells used in this study. Specifically, they could also be used for investigating all-organic solid-state batteries such as the recently reported and very promising cells comprising polymeric anode and cathode materials as well as gel electrolytes based on ionic liquids.<sup>48</sup> In particular, low-temperature spin-echo experiments also hold promise for elucidating electron transfer processes in redox flow batteries.<sup>38</sup>

A strategy for overcoming sensitivity limitations of advanced EPR experiments is to combine them with electrical readout schemes and make Electrically Detected Magnetic Resonance (EDMR) applicable to study redox and transport processes in polymer batteries. EDMR possesses a sensitivity many orders of magnitude higher than conventional EPR measurements.<sup>49</sup> The possibility of using EDMR techniques for battery characterization at ambient conditions would also open up entirely new opportunities for imaging techniques. EDMR imaging could provide a detailed picture of the spatial distribution of active and inactive redox centres and, in general, usefully complement information obtained through imaging techniques based on conventional EPR<sup>50–52</sup> or nuclear magnetic resonance.<sup>53</sup>

## Conflicts of interest

There are no conflicts to declare.

## Acknowledgements

This work was supported by the joint RSF-DFG grant program (RSF grant number 22-43-04414, DFG grant number BE 5126/7-1). We further acknowledge financial support from the German-Russian Interdisciplinary Science Center (G-RISC) funded by the German Federal Foreign Office *via* the German Academic Exchange Service (DAAD). Academic exchange between Saint-Petersburg State University and Freie Universität Berlin was supported by a Joint Seed Funding Project (grant number 39855834).

## Notes and references

- 1 K. Nakahara, S. Iwasa, M. Satoh, Y. Morioka, J. Iriyama, M. Suguro and E. Hasegawa, *Chem. Phys. Lett.*, 2002, **359**, 351–354.
- 2 H. Nishide, S. Iwasa, Y. J. Pu, T. Suga, K. Nakahara and M. Satoh, *Electrochim. Acta*, 2004, **50**, 827–831.
- 3 Y. Xie, K. Zhang, Y. Yamauchi, K. Oyaizu and Z. F. Jia, *Mater. Horiz.*, 2021, **8**, 803–829.
- 4 P. Rohland, E. Schröter, O. Nolte, G. R. Newkome, M. D. Hager and U. S. Schubert, *Prog. Polym. Sci.*, 2022, **125**, 101474.
- 5 T. Janoschka, M. D. Hager and U. S. Schubert, *Adv. Mater.*, 2012, **24**, 6397–6409.
- 6 S. Muench, A. Wild, C. Friebe, B. Haupler, T. Janoschka and U. S. Schubert, *Chem. Rev.*, 2016, **116**, 9438–9484.
- 7 C. Friebe and U. S. Schubert, *Top. Curr. Chem.*, 2017, **375**, 19.
- 8 K. Oyaizu, H. Tatsuhira and H. Nishide, *Polym. J.*, 2015, **47**, 212–219.
- 9 S. Bahceci and B. Esat, *J. Power Sources*, 2013, **242**, 33–40.
- 10 T. Katsumata, M. Satoh, J. Wada, M. Shiotsuki, F. Sanda and T. Masuda, *Macromol. Rapid Commun.*, 2006, **27**, 1206–1211.
- 11 L. H. Xu, F. Yang, C. Su, L. L. Ji and C. Zhang, *Electrochim. Acta*, 2014, **130**, 148–155.
- 12 M. Aydin and B. Esat, *J. Solid State Electrochem.*, 2015, **19**, 2275–2281.
- 13 P. O. Schwartz, M. Pejic, M. Wachtler and P. Bauerle, *Synth. Met.*, 2018, **243**, 51–57.
- 14 M. Khodeir, B. Ernould, J. Brassinne, S. Ghiassinejad, H. Jia, S. Antoun, C. Friebe, U. S. Schubert, Z. Kochovski, Y. Lu, E. V. Ruybeke and J. F. Gohy, *Soft Matter*, 2019, **15**, 6418–6426.
- 15 Y. Zhang, A. M. Park, S. R. McMillan, N. J. Harmon, M. E. Flatté, G. D. Fuchs and C. K. Ober, *Chem. Mater.*, 2018, **30**, 4799–4807.
- 16 Q. Huang, E. D. Walter, L. Cosimbescu, D. Choi and J. P. Lemmon, *J. Power Sources*, 2016, **306**, 812–816.
- 17 Y. Kanzaki, S. Mitani, D. Shiomi, Y. Morita, T. Takui and K. Sato, *ACS Appl. Mater. Interfaces*, 2018, **10**, 43631–43640.
- 18 M. Arvind, C. E. Tait, M. Guerrini, J. Krumland, A. M. Valencia, C. Cocchi, A. E. Mansour, N. Koch, S. Barlow, S. R. Marder, J. Behrends and D. Neher, *J. Phys. Chem. B*, 2020, **124**, 7694–7708.



- 19 P. Pingel, M. Arvind, L. Kolln, R. Steyrleuthner, F. Kraffert, J. Behrends, S. Janietz and D. Neher, *Adv. Electron. Mater.*, 2016, **2**, 1600204.
- 20 J. Wandt, C. Marino, H. A. Gasteiger, P. Jakes, R. A. Eichel and J. Granwehr, *Energy Environ. Sci.*, 2015, **8**, 1358–1367.
- 21 B. Wang, L. W. L. Fevre, A. Brookfield, E. J. L. McInnes and R. A. W. Dryfe, *Angew. Chem., Int. Ed.*, 2021, **2**–11.
- 22 M. X. Tang, A. Dalzini, X. Li, X. Y. Feng, P. H. Chien, L. K. Song and Y. Y. Hu, *J. Phys. Chem. Lett.*, 2017, **8**, 4009–4016.
- 23 H. Nguyen and R. J. Clement, *ACS Energy Lett.*, 2020, **5**, 3848–3859.
- 24 M. G. Santangelo, M. Levantino, A. Cupane and G. Jeschke, *J. Phys. Chem. B*, 2008, **112**, 15546–15553.
- 25 A. Clark, J. Sedhom, H. Elajaili, G. R. Eaton and S. S. Eaton, *Concepts Magn. Reson., Part A*, 2016, **45a**, e21423.
- 26 A. Schweiger and G. Jeschke, *Principles of pulse electron paramagnetic resonance*, Oxford University Press, Oxford, UK, New York, 2001.
- 27 C. Szczuka, J. Ackermann, P. P. M. Schleker, P. Jakes, R. A. Eichel and J. Granwehr, *Commun. Mater.*, 2021, **2**, 20.
- 28 G. Jeschke, *Annu. Rev. Phys. Chem.*, 2012, **63**, 419–446.
- 29 R. Steyrleuthner, Y. X. Zhang, L. Zhang, F. Kraffert, B. P. Cherniawski, R. Bittl, A. L. Briseno, J. L. Bredas and J. Behrends, *Phys. Chem. Chem. Phys.*, 2017, **19**, 3627–3639.
- 30 E. Bordignon, *eMagRes*, 2017, **6**, 235–253.
- 31 A. A. Vereshchagin, D. A. Lukyanov, I. R. Kulikov, N. A. Panjwani, E. A. Alekseeva, J. Behrends and O. V. Levin, *Batteries Supercaps*, 2021, **4**, 336–346.
- 32 K. Abdiaziz, E. Salvadori, K. P. Sokol, E. Reisner and M. M. Roessler, *Chem. Commun.*, 2019, **55**, 8840–8843.
- 33 Y. Kutin, N. Cox, W. Lubitz, A. Schnegg and O. Rüdiger, *Catalysts*, 2019, **9**, 926.
- 34 S. Neukermans, M. Samanipour, H. Y. V. Ching, J. Hereijgers, S. V. Doorslaer, A. Hubin and T. Breugelmans, *ChemElectroChem*, 2020, **7**, 4578–4586.
- 35 S. A. Bonke, T. Risse, A. Schnegg and A. Brückner, *Nat. Rev. Methods Primers*, 2021, **1**, 33.
- 36 J. B. Priebe, M. Karnahl, H. Junge, M. Beller, D. Hollmann and A. Brückner, *Angew. Chem., Int. Ed.*, 2013, **52**, 11420–11424.
- 37 J. Rabeah, U. Bentrup, R. Stösser and A. Brückner, *Angew. Chem., Int. Ed.*, 2015, **54**, 11791–11794.
- 38 E. W. Zhao, E. Jonsson, R. B. Jethwa, D. Hey, D. X. Lyu, A. Brookfield, P. A. A. Klusener, D. Collison and C. P. Grey, *J. Am. Chem. Soc.*, 2021, **143**, 1885–1895.
- 39 J. D. Wadhawan and R. G. Compton, in *Encyclopedia of Electrochemistry*, ed. A. J. Bard and M. Stratmann, Wiley, New York, 2007, p. 170.
- 40 S. Safari, P. R. Selvaganapathy, A. Derardja and M. J. Deen, *Nanotechnology*, 2011, **22**, 315601.
- 41 D. F. Liu, X. Q. Lü and R. Lu, *Transition Met. Chem.*, 2014, **39**, 705–712.
- 42 A. N. Yankin, D. A. Lukyanov, E. Beletskii, O. Y. Bakulina, P. S. Vlasov and O. V. Levin, *ChemistrySelect*, 2019, **39**, 8886–8890.
- 43 E. Dmitrieva, M. Rosenkranz, J. S. Danilova, E. A. Smirnova, M. P. Karushev, I. A. Chepurnaya and A. M. Timonov, *Electrochim. Acta*, 2018, **283**, 1742–1752.
- 44 P. W. Anderson and P. R. Weiss, *Rev. Mod. Phys.*, 1953, **25**, 269–276.
- 45 X. Liu, Y. Mao, E. V. Mathias, C. Ma, O. Franco, Y. Ba, J. A. Kornfield, T. Wang, L. Xue, B. S. Zhou and Y. Yen, *J. Sol-Gel Sci. Technol.*, 2008, **45**, 269–278.
- 46 S. Stoll and A. Schweiger, *J. Magn. Reson.*, 2006, **178**, 42–55.
- 47 M. Toybenshlak and R. Carmieli, *Isr. J. Chem.*, 2019, **59**, 1020–1026.
- 48 S. M. Muench, R. Burges, A. Lex-Balducci, J. C. Brendel, M. Jager, C. Friebe, A. Wild and U. S. Schubert, *J. Polym. Sci.*, 2021, **59**, 494–501.
- 49 D. R. McCamey, H. Huebl, M. S. Brandt, W. D. Hutchison, J. C. McCallum, R. G. Clark and A. R. Hamilton, *Appl. Phys. Lett.*, 2006, **89**, 182115.
- 50 M. Sathiya, J. B. Leriche, E. Salager, D. Gourier, J. M. Tarascon and H. Vezin, *Nat. Commun.*, 2015, **6**, 6276.
- 51 C. E. Dutoit, M. X. Tang, D. Gourier, J. M. Tarascon, H. Vezin and E. Salager, *Nat. Commun.*, 2021, **12**, 1410.
- 52 F. S. Geng, Q. Yang, C. Li, M. Shen, Q. Chen and B. W. Hu, *Chem. Mater.*, 2021, **33**, 8223–8234.
- 53 A. J. Illott, M. Mohammadi, H. J. Chang, C. P. Grey and A. Jerschow, *Proc. Natl. Acad. Sci. U. S. A.*, 2016, **113**, 10779–10784.

